X-ray Diffraction & Elemental Analysis

# THE BRIDGE

MATERIALS ANALYSIS eNEWSLETTER
MARCH 2014, ISSUE 9



## Welcome

Pittcon, the large analytical instrument show in the U.S., has come and gone for another year. As always it is interesting to see what is new in the instrumentation arena, and one trend that continues to progress is the downsizing of analytical instruments. As an example, Rigaku introduced a new handheld Raman spectrometer, the Progeny, which has been specifically designed to be customizable and flexible for seamless integration into any work environment.

The tradeshow season is now in full swing and Rigaku will be at meetings all over the world this month. Please stop by and see us if you happen to attend one of the shows where we are exhibiting.

Enjoy the newsletter.

A bridge is often used to symbolize a connection or link between two places, and thus we felt The Bridge would be the perfect name for our eNewsletter, as we hope that it will act as a vehicle for the transmission of ideas and information between Rigaku and interested readers around the world.

And a bridge is a two-way structure, a concept that we will keep in mind as we not only provide information about Rigaku, but also report on interesting research and the associated laboratories around the world, publish technical book reviews that might help our readers in their work, and highlight general news topics that are of interest to many people involved in materials analysis.

*Photo by Paul Swepston*

Progeny™

## Advanced handheld Raman spectrometer

**1064 nm laser for superior Raman performance**

From the evolution of handheld spectroscopy comes Progeny, the first handheld Raman analyzer designed to be customizable and flexible for seamless integration into any work environment. Now you can perform lab-quality analysis of the widest range of solids, powders, liquids, and other substances to ensure consumer safety around the globe.

Click here for more information

## Customer in the Spotlight

**Rigaku 3D micro X-ray CT for Laboratory Animals in Laboratory of Cell and Tissue Biology**

School of Medicine, Keio University

Prof. Koichi Matsuo, MD, PhD is researching bone cell interactions and mechanisms of bone morphogenesis. X-ray imaging–such as TEM, SEM and MRI–is an effective tool for the study of cells, including bone and tissue biology. Prof. Koichi Matsuo installed the first instrument in 2009 not only for his research but also as a shared research instrument in the School of Medicine, Keio University. Recently, the second Rigaku X-ray micro CT has been installed.

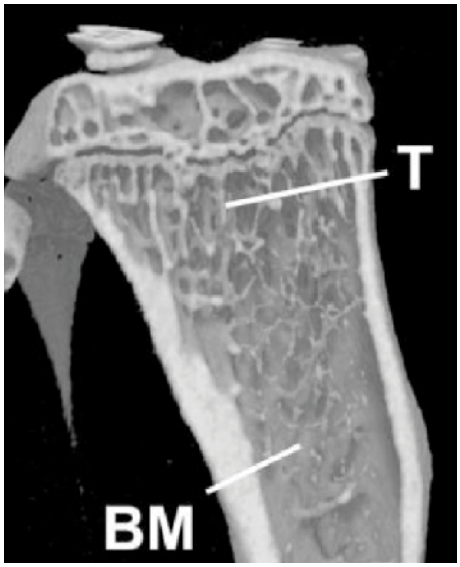


This micro CT instrument can measure the kinetic events in real time utilizing a fluoroscopy mode. It is also possible to determine the longitudinal temporal change of the sample.

The figure above is a view of bone interior, inside an adult mouse tibia, measured by micro X-ray CT. The symbol "T" indicates the trabecular structure and "BM" indicates bone marrow cavity.

Prof. Matsuo's team can trace the temporal change of T and BM using the Rigaku micro X-ray CT.

The users of this instrument are researchers in many departments and divisions such as, Molecular Biology, Preventive Medicine, Pharmacology, Neuroscience, Orthopedics, and Internal Medicine. The School of Medicine, Keio Univ., is well known for the founder, Shibasaburo Kitasato, and moreover for the neural stem cell researcher, Prof. Hideyuki Okano, who is a pioneer of this field in Japan. For Prof. Okano's research, the Rigaku micro CT has been used for checking the remodeling of spinal marrow.

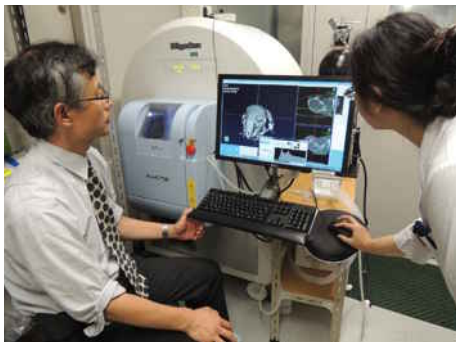

***Prof. Matsuo (left) at the Rigaku micro X-ray CT***

***Prof. Matsuo (right) and technical scientist and sales person***

# Scientific Book Review

***The Theory that Would Not Die: How Bayes' Rule Cracked the Enigma Code, Hunted Down Russian Submarines & Emerged Triumphant from Centuries of Controversy***
**By Sharon Bertsch McGrayne**

Yale University Press, 2011, 336 pages, ISBN: 978-0-300-18822-6

"It was a matter of applying Bayes' Theorem to estimate the conditional probabilities. Giving due weight to the *prior* probabilities and …" No, this is not from a lecture by Gerard Bricogne but from a Robert Ludlum novel, *The Ambler Warning* (2005). I thought this would be a good way to demonstrate how pervasive Bayes' Theorem has become.

The book starts off naturally with a short biography of Reverend Thomas Bayes and a simple statement of the theorem that bears his name: prior times likelihood is proportional to the posterior. We learn Bayes made some errors in convincing others of the validity of the theorem because the prior must often be a guess and scientists did not like the subjective nature of this starting point. The next chapter covers the rederivation of Bayes' Theorem by Pierre Simon Laplace and how he used it resolve the issues of the stability of the solar system, among many other problems. In the third chapter, we learn how Bayes' Theorem almost died at the hands of the frequentists yet managed to survive.

Next the author fastforwards to WWII, in which Alan Turing and his team at Bletchley Park used Bayes' Theorem to decode Enigma. We are next introduced to Arthur Bailey, an insurance actuary, who used Bayes to predict the probability of airplane accidents, and Jerome Cornfield a researcher at NIH, to show the correlation between smoking and lung cancer in the 1950s.

One of the strengths of Bayes is the ability to predict probabilities when there are no frequency data at all. So, Jimmie Savage used Bayes to help the Air Force comes to terms with the very real probability that something bad could happen with all the bombs flying around in B-52s in the 50s and 60s. To his credit, Curtis LeMay changed Air Force operations in accordance with Bayes.

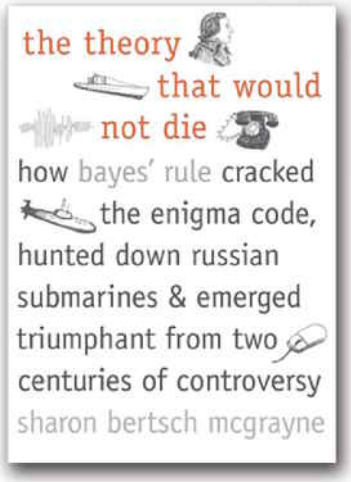


There are so many examples of how Bayes has solved difficult problems that frequency based statistics could not: finding Russian submarines that went missing, finding a lost atomic bomb after a mid-air refueling accident, determining the author of *The Federalist*, helping Google Translate translate and finding the final resting place of Air France 447.

This is one of those books that I probably would never have found without perusing stacks at a bookstore. This book is a real gem and reads with the speed of a spy novel. The history and application of Bayes' Theorem is brought out in clear, easy to understand language with detailed footnotes and an extensive bibliography. A humorous piece on religion and Bayes by Michael J. Campbell and some simple, real life, examples are provided in the appendices.

***Joseph D. Ferrara, Ph.D.***
***Chief Science Officer, Rigaku***


# Conferences

Rigaku exhibited March 2 – 6 (photo above) at PITTCON 2014 in Chicago, IL, USA.

Rigaku will be sponsoring, attending or exhibiting at the following conferences and trade shows:

**American Chemical Society – Spring Meeting**
Dallas, TX, USA
*March 16 – 20*

**JSAP EXPO Spring**
Kanagawa, Japan
*March 17 – 20*

**DGK**
Berlin, Germany
*March 17 – 20*

**ARABLAB**
Dubai
*March 17 – 20*

Click here to see the complete list

## Benchtop qualitative and quantitative powder diffraction

**Video in the spotlight**

The benefits of WDXRF, light element sensitivity and high spectral resolution, in a benchtop instrument. The Supermini200 is about ½ the price and ¼ the size of conventional WDXRF systems.

Click here for more information on the Rigaku Supermini200

# Material Analysis in the News

**March 3, 2014.** Metals and nanomechanics expert Ying Chen, Assistant Professor in the Department of Materials Science and Engineering at Rensselaer Polytechnic Institute, has won a prestigious Faculty Early Career Development Award (CAREER) from the National Science Foundation (NSF). Chen will use the five-year, $540,000 grant to study and develop "smart metals" informed by leading-edge interface engineering. Known as shape memory alloys (SMAs), these smart metals can return to their original shape after being changed or deformed.

**March 6, 2014.** A new Center for Dielectrics and Piezoelectrics, supported by the National Science Foundation and co-located at Penn State and North Carolina State University, will build on and expand the research capabilities of Penn State's long-running Center for Dielectrics Studies. The new center is an NSF multi-university Industry/University Cooperative Research Center, with 18 inaugural industry partners. The NSF will provide $830,000 over five years to support operations and infrastructure, with additional funding coming from member companies and organizations.

**March 7, 2014.** Researchers have now taken a first step toward using X-rays to obtain precise structures and observe the reaction dynamics of individual gas-phase molecules, reports an international team. The technique was developed by a team led by Jochen Küpper, leader of the controlled molecule imaging group at Germany's Centre for Free-Electron Laser Science, which is affiliated with the DESY synchrotron accelerator center.

**March 7, 2014.** The International Space Station (ISS) is set to do a spot of industrial research this June, when ESA's Materials Science Laboratory-Electromagnetic Levitator (MSL-EML) heads for the station aboard Europe's' Automated Transfer Vehicle 5 (ATV-5) Georges Lemaître unmanned space freighter as part of a program to study the casting of alloys in a weightless environment. By means of microgravity, scientists hope to gain a better understanding of an alloy's surface tension, viscosity, melting range, fraction solid, specific heat, heat of fusion, mass density, and thermal expansion among other things.

**March 10, 2014.** Researchers at the Vienna University of Technology have succeeded in creating a diode made of tungsten diselenide. Experiments show that this material may be used to create ultrathin flexible solar cells. Even flexible displays could become possible. Tungsten diselenide consists of one layer of tungsten atoms, which are connected by selenium atoms above and below the tungsten plane. The material absorbs light, much like graphene, but in tungsten diselenide, this light can be used to create electrical power.

**March 11, 2014.** When ORNL scientists Kai Xiao and Kunlun Hong analyzed neutron scattering data obtained at the lab's Spallation Neutron Source to measure the structure of seemingly identical polymer-based solar devices, they stumbled upon a new piece to the scientific solar puzzle. Scientists usually assume that the deuteration doesn't change the electronic structure of polymers, but when it was used to study conducting polymers in solar cells, the devices' electronic performance was found to have changed significantly.

**March 11, 2014.** Organic solar cells are a compelling thin-film photovoltaic technology in part because of their compatibility with flexible substrates and tunable absorption window. Belgium-based chipmaker IMEC has set a new conversion efficiency record of 8.4% for this type of cell by developing fullerene-free acceptor materials and a new multilayer semiconductor device structure.

**March 12, 2014.** Researchers have discovered that creating a graphene-copper-graphene "sandwich" strongly enhances the heat conducting properties of copper, a discovery that could further help in the downscaling of electronics. The work was led by Alexander A. Balandin, a professor of electrical engineering at the Bourns College of Engineering at the Univ. of California, Riverside and Konstantin S. Novoselov, a professor of physics at the Univ. of Manchester in the United Kingdom.

**March 13, 2014.** Maney Publishing today announces the launch of four new materials science and engineering journals. The journals will cover the rapidly developing subject areas of nanocomposites, the use of polymers and composites in advanced manufacturing, structure-function relationships in catalytic science, and the use of advanced materials for optical, sensing and acoustic devices.

**March 13, 2014.** The team of Francesca Ferlaino, at the Institute for Experimental Physics of the Univ. of Innsbruck, Austria, has experimentally shown chaotic behavior of particles in a quantum gas. They were able to observe quantum chaos in the scattering behavior of ultracold atoms. The physicists used random matrix theory to confirm their results, thus asserting the universal character of this statistical theory.

# The Adventures of Captain Nano

**DIFFERENT EFFECTS** — Dr. F. Furter's so-called brilliant mind conjures up a different way to duplicate our hero's experiment.

# Recent Scientific Papers of Interest

**Defects and acceptor centers in ZnO introduced by C-implantation.** Jiang, M.; Xue, X.; Chen, Z.; Liu, Y.; Liang, H.; Zhang, H.; Kawasuso, A. Journal of Materials Science. Mar2014, Vol. 49 Issue 5, p1994-1999. 6p. 6 Graphs. DOI: 10.1007/s10853-013-7886-4.

**Effect of fibre spinning conditions on the electrical properties of cellulose and carbon nanotube composite fibres spun using ionic liquid as a benign solvent.** Zhu, C.; Chen, J.; Koziol, K. K.; Gilman, J. W.; Trulove, P. C.; Rahatekar, S. S. Express Polymer Letters. 2014, Vol. 8 Issue 3, p154-163. 10p. 2 Black and White Photographs, 1 Diagram, 1 Chart, 5 Graphs. DOI: 10.3144/expresspolymlett.2014.19.

**Application of confocal technology based on polycapillary X-ray optics in three-dimensional diffraction scanning analysis.** Sun, Tianxi; Liu, Hehe; Liu, Zhiguo; Peng, Song; Ma, Yongzhong; Sun, Weiyuan; Luo, Ping; Ding, Xunliang. Nuclear Instruments & Methods in Physics Research Section B. Mar2014, Vol. 323, p25-29. 5p. DOI: 10.1016/j.nimb.2014.01.013.

**Moganite in selected Polish chert samples: The evidence from MIR, Raman and X-ray studies.** Sitarz, M.; Wyszomirski, P.; Handke, B.; Jeleń, P. Spectrochimica Acta Part A: Molecular & Biomolecular Spectroscopy. Mar2014, Vol. 122, p55-58. 4p. DOI: 10.1016/j.saa.2013.11.039.

**Particle size effect on thermal conductivity of AlN films with embedded diamond particles.** Pan, T.; Zhang, Y.; Huang, J.; Gao, M.; Lin, Y. Applied Physics A: Materials Science & Processing. Mar2014, Vol. 114 Issue 3, p973-978. 6p. DOI: 10.1007/s00339-013-8045-0.

**A small-angle X-ray scattering station at Beijing synchrotron radiation facility.** Li, Zhihong; Wu, Zhonghua; Mo, Guang; Xing, Xueqing; Liu, Peng. Instrumentation Science & Technology. Mar/Apr2014, Vol. 42 Issue 2, p128-141. 14p. DOI: 10.1080/10739149.2013.845845.

**Monte Carlo simulation of X-ray imaging and spectroscopy experiments using quadric geometry and variance reduction techniques.** Golosio, Bruno; Schoonjans, Tom; Brunetti, Antonio; Oliva, Piernicola; Masala, Giovanni Luca. Computer Physics Communications. Mar2014, Vol. 185 Issue 3, p1044-1052. 9p. DOI: 10.1016/j.cpc.2013.10.034.

**Kinetics of the chrysotile and brucite dehydroxylation reaction: a combined non-isothermal/isothermal thermogravimetric analysis and high-temperature X-ray powder diffraction study.** Trittschack, Roy; Grobéty, Bernard; Brodard, Pierre. Physics & Chemistry of Minerals. Mar2014, Vol. 41 Issue 3, p197-214. 18p. DOI: 10.1007/s00269-013-0638-9.

**Residual Stresses Comparison Determined by Short-Wavelength X-Ray Diffraction and Neutron Diffraction for 7075 Aluminum Alloy.** Zhang, Jin; Zheng, Lin; Guo, XueBo; Ji, Vincent; Klosek, Vincent. Journal of Nondestructive Evaluation. Mar2014, Vol. 33 Issue 1, p82-92. 11p. DOI: 10.1007/s10921-013-0205-9.

**Comparative study of gamma ray shielding and some properties of $PbO–SiO_2–Al_2O_3$ and $Bi_2O_3–SiO_2–Al_2O_3$ glass systems.** Singh, K.J.; Kaur, Sandeep; Kaundal, R.S. Radiation Physics & Chemistry. Mar2014, Vol. 96, p153-157. 5p. DOI: 10.1016/j.radphyschem.2013.09.015.

**Microstructure evolution of heavily deformed AA5083 Al–Mg alloy studied by positron annihilation spectroscopy.** Zou, B.; Chen, Z.Q.; Liu, C.H.; Chen, J.H. Applied Surface Science. Mar2014, Vol. 296, p154-157. 4p. DOI: 10.1016/j.apsusc.2014.01.064.

**Characterization of $La_{2-x}Sr_xCoTiO_6$ ($0.6 \leq x \leq 1.0$) series as new cathodes of solid oxide fuel cells.** Pérez-Flores, Juan Carlos; Gómez-Pérez, Alejandro; Yuste, Mercedes; Canales-Vázquez, Jesús; Climent-Pascual, Esteban; Ritter, Clemens; Azcondo, M. Teresa; Amador, Ulises; García-Alvarado, Flaviano. International Journal of Hydrogen Energy. Mar2014, Vol. 39 Issue 10, p5440-5450. 11p. DOI: 10.1016/j.ijhydene.2014.01.058.

**Micro-deformation mechanism of Zr-based metallic glass/porous tungsten composite by *in-situ* high-energy X-ray diffraction and finite element modeling.** Zhang, X.Q.; Wang, L.; Fan, Q.B.; Xue, Y.F.; Wang, Y.D.; Nie, Z.H.; Zhang, H.F.; Fu, H.M. Materials Science & Engineering: A. Mar2014, Vol. 598, p407-412. 6p. DOI: 10.1016/j.msea.2014.01.057.

**Assessment of dislocation density in asymmetrically cyclic loaded non-conventional stainless steel using X-ray diffraction profile analysis.** Kishor, Rajat; Sahu, Lopamudra; Dutta, Krishna; Mondal, A.K. Materials Science & Engineering: A. Mar2014, Vol. 598, p299-303. 5p. DOI: 10.1016/j.msea.2014.01.043.

**Characterization of crystallite size, dislocation characteristics and stacking faults in nanostructured mechanically alloyed Cu–Fe system using an advanced X-ray diffraction analysis method.** Soleimanian, V.; Mojtahedi, M.; Goodarzi, M.; Aboutalebi, M.R. Journal of Alloys & Compounds. Mar2014, Vol. 590, p565-571. 7p. DOI: 10.1016/j.jallcom.2013.12.067.

**Development and application of variable-magnification x-ray Bragg magnifiers.** Hirano, K.; Takahashi, Y.; Sugiyama, H. Nuclear Instruments & Methods in Physics Research Section A. Mar2014, Vol. 741, p78-83. 6p. DOI: 10.1016/j.nima.2013.12.038.

**Research on annealing and properties of TlBr crystals for radiation detector use.** Zhiping, Zheng; Yongtao, Yu; Dongxiang, Zhou; Shuping, Gong; Qiuyun, Fu. Nuclear Instruments & Methods in Physics Research Section A. Mar2014, Vol. 741, p104-107. 4p. DOI: 10.1016/j.nima.2013.12.049.

**Diffraction and spectroscopic study of pyrochlores $Bi_{2-x}Fe_{1+x}SbO_7$.** Zhou, Qingdi; Blanchard, Peter E.R.; Kennedy, Brendan J.; Ling, Chris D.; Liu, Samuel; Avdeev, Max; Aitken, Jade B.; Tadich, Anton; Brand, Helen E.A. Journal of Alloys & Compounds. Mar2014, Vol. 589, p425-430. 6p. DOI: 10.1016/j.jallcom.2013.11.226.

**An *in situ* synchrotron X-ray diffraction study of precipitation kinetics in a severely deformed Cu–Ni–Si alloy.** Azzeddine, H.; Mehdi, B.; Hennet, L.; Thiaudière, D.; Alili, B.; Kawasaki, M.; Bradai, D.; Langdon, T.G. Materials Science & Engineering: A. Mar2014, Vol. 597, p288-294. 7p. DOI: 10.1016/j.msea.2013.12.092.

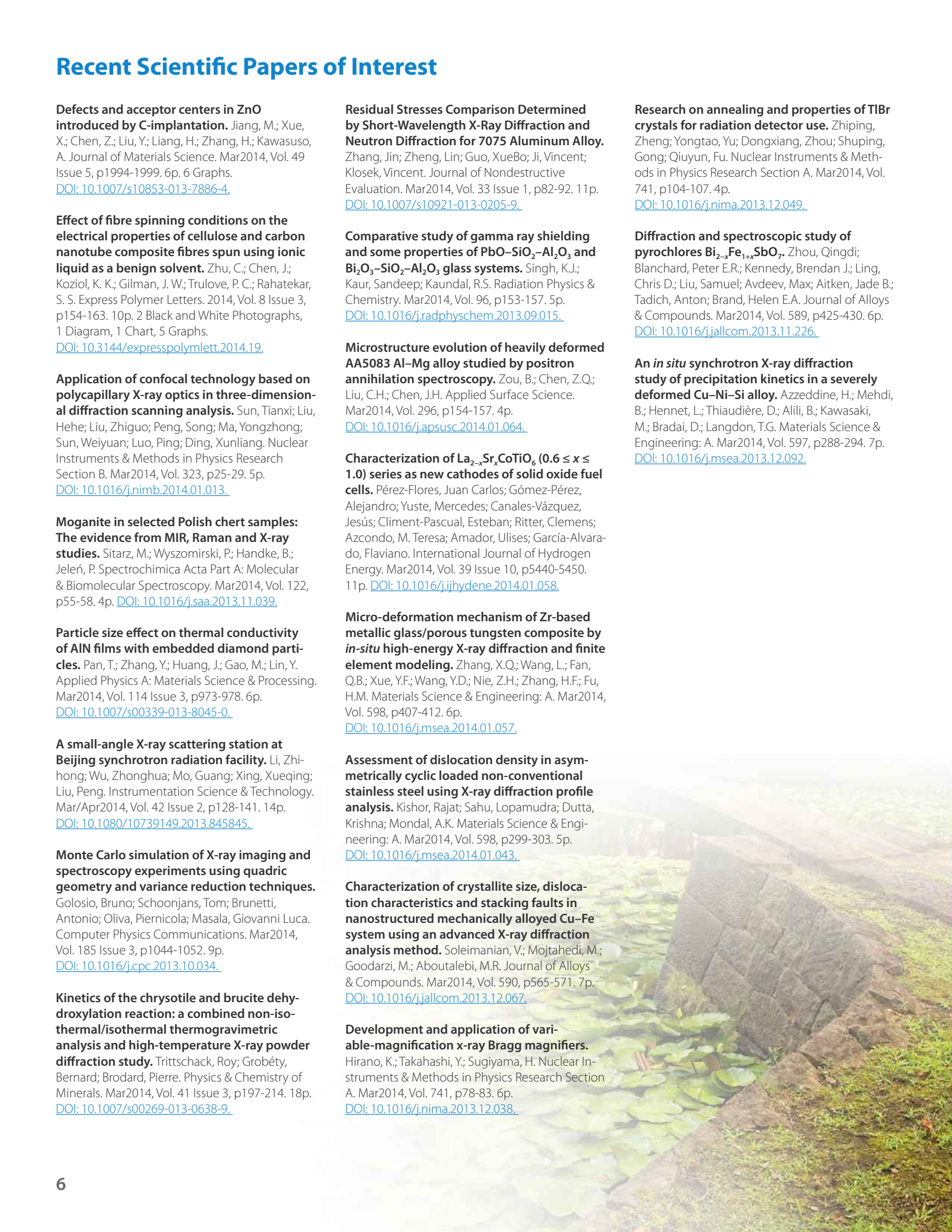

# EDXRF Application Note
## Analysis of S, V, Ni
## in Crude Oil
#1323

### SCOPE
The analysis of sulfur, vanadium and nickel in crude oil is demonstrated.


### BACKGROUND
Sulfur, vanadium and nickel occur naturally in crude oil, and their concentrations vary depending on the geographical region of the oil deposits. Vanadium and nickel can foul the refining process during crude oil cracking, and so crude oil with low levels of vanadium and nickel is desirable. In the oil fields and in off-shore drilling, a quick and easy means of screening for vanadium and nickel is a valuable tool to begin to characterize the quality of the crude before refining. Applied Rigaku Technologies meets the industry analytical need with the NEX QC series of EDXRF analyzers. Fast and simple, the NEX QC$^+$ provides an ideal tool for monitoring the concentrations of vanadium and nickel in crude, as well as the sulfur content.

### INSTRUMENTATION

| | |
|---|---|
| **Model:** | Rigaku NEX QC$^+$ |
| **X-ray tube:** | 4 W Ag-anode |
| **Detector:** | SDD |
| **Sample Type**: | Crude Oil |
| **Film:** | Mylar |
| **Analysis Time:** | 460 sec |
| **Environment:** | Air |
| **Optional:** | Single Position or Autosampler |


### SAMPLE PREPARATION
Ensure each oil sample is homogeneous and stable. Simply fill an XRF sample cup 3/4 full (5g) and measure directly.

Applied Rigaku Technologies, Inc. • 9825 Spectrum Drive, Bldg. 4, Suite 475 • Austin, TX 78717 USA
www.RigakuEDXRF.com • info@RigakuEDXRF.com • (+1) 512-225-1796

## CALIBRATION

Empirical calibrations were built using a suite of 10 commercially available mineral oil calibration standards that represent crude oil.

| Element | Concentration Range | RMS Deviation | $R^2$ Confidence |
|---|---|---|---|
| S | 0.30 – 4.00 % | 0.026 | 0.99965 |
| V | 5 – 50 ppm | 0.5 | 0.99936 |
| Ni | 3 – 50 ppm | 0.9 | 0.99897 |

## REPEATABILITY

To demonstrate repeatability (precision), two calibration standards were measured in 10 repeat analyses using an analysis time of 460 sec per sample without moving the sample between measurements.

| Sample: Std 8 | | | | |
|---|---|---|---|---|
| Element | Standard Value | Average Value | Std Dev | % Relative Dev |
| S | 3.202 % | 3.200 % | 0.023 | 0.7 |
| V | 40.1 ppm | 40.1 ppm | 0.3 | 0.7 |
| Ni | 5.0 | 4.9 | 0.9 | --- |

| Sample: Std 3 | | | | |
|---|---|---|---|---|
| Element | Standard Value | Average Value | Std Dev | % Relative Dev |
| S | 1.152 % | 1.159 % | 0.010 | 0.3 |
| V | 5.0 ppm | 4.8 ppm | 0.3 | --- |
| Ni | 45.1 | 45.6 | 0.4 | 0.9 |

## DETECTION LIMITS (LLD – Lower Limit of Detection)

In the empirical method, ten repeat analyses of a blank mineral oil sample are taken with the sample in static position, and the standard deviation ($\sigma$) is determined. The LLD (Lower Limit of Detection) is then defined as $3\sigma$. Increasing the measurement time can lower detection limits.

| 460 sec analysis time | |
|---|---|
| Element | LLD |
| S | 0.003 % |
| V | 0.6 ppm |
| Ni | 1.5 ppm |



Applied Rigaku Technologies, Inc. • 9825 Spectrum Drive, Bldg. 4, Suite 475 • Austin, TX 78717 USA
www.RigakuEDXRF.com • info@RigakuEDXRF.com • (+1) 512-225-1796

## SPECTRA

The spectra here demonstrate the multi-element capability of the NEX QC+ for analyzing crude oils.

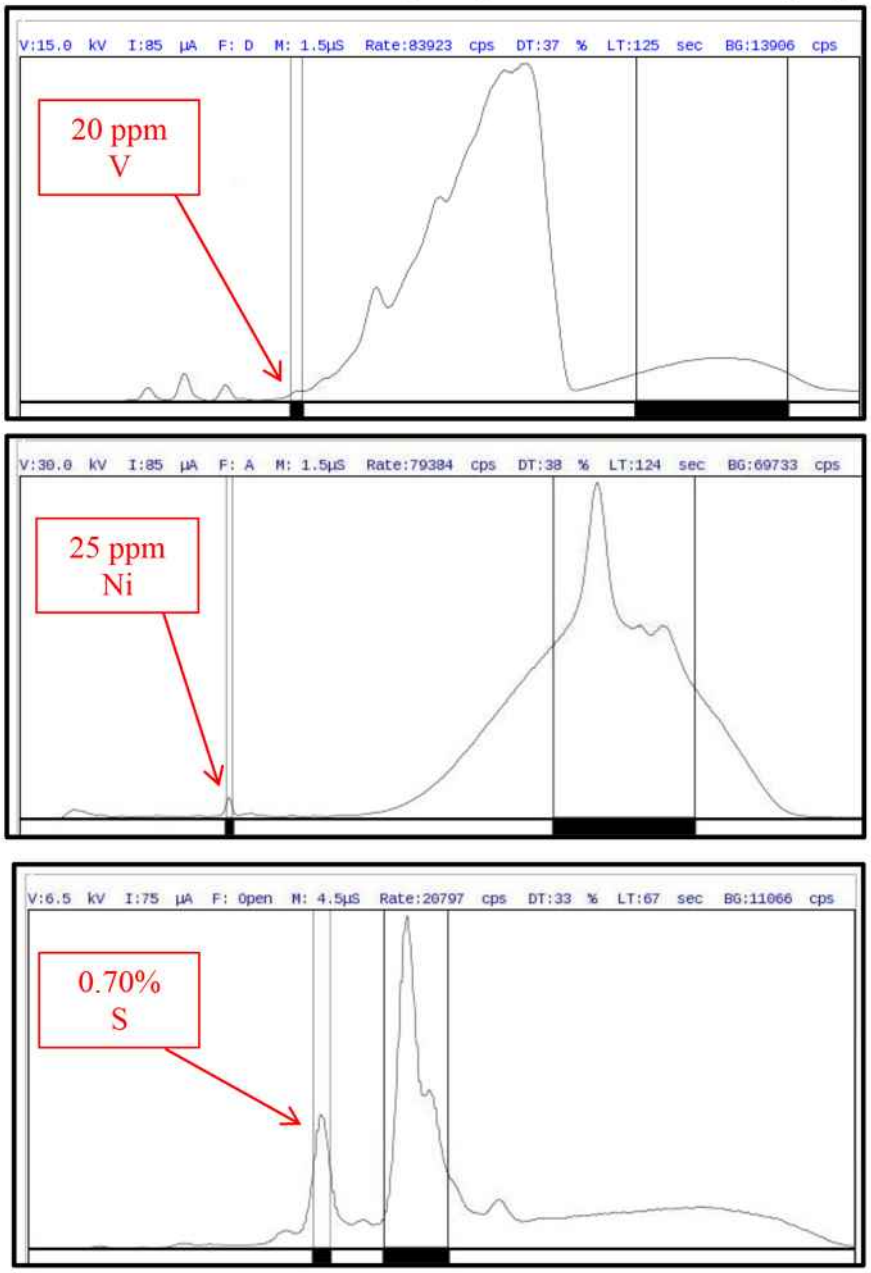


## CONCLUSION

The NEX QC$^+$ offers analysts a simple yet powerful and versatile system for quantifying elemental composition using the empirical approach. The results of this study indicate that given stable samples, proper sample handling and proper calibration technique, the Rigaku NEX QC$^+$ EDXRF can achieve excellent results in monitoring the concentration of sulfur, vanadium and nickel in oil.



Applied Rigaku Technologies, Inc. • 9825 Spectrum Drive, Bldg. 4, Suite 475 • Austin, TX 78717 USA
www.RigakuEDXRF.com • info@RigakuEDXRF.com • (+1) 512-225-1796

Rigaku

# X-ray Diffraction Analysis for Thin Film Samples

Training Textbook

As shown in Fig. 2.3.9, the change or fluctuation in interplanar spacing and the change or fluctuation in crystal lattice orientation affect the position and spread of the reciprocal lattice point in different ways. We can isolate these aspects of the crystal structure by measuring these changes.

## 2.4 Reciprocal Lattice and Measurement Axes

The sections up to this point have discussed the relationship between the crystal lattice and the reciprocal lattice and the method of expressing the diffraction condition. We have also found that a change in crystal structure and crystallinity is observed as a change in the position or shape of the reciprocal lattice point. However, when measuring the position or shape of the reciprocal lattice point in practical measurements to evaluate crystal structure or the crystallinity, we need to understand the relationship between the reciprocal lattice and the measurement axes. This section discusses the relationship between the rotation axes of the sample or of the goniometer and the reciprocal lattice.

### 2.4.1 Four-Circle Goniometer

In the goniometers typically used to measure single crystals or strongly oriented polycrystals, the rotation axes of the sample and the counter, or the rotation axes of the goniometer, are defined as in Fig. 2.4.1.

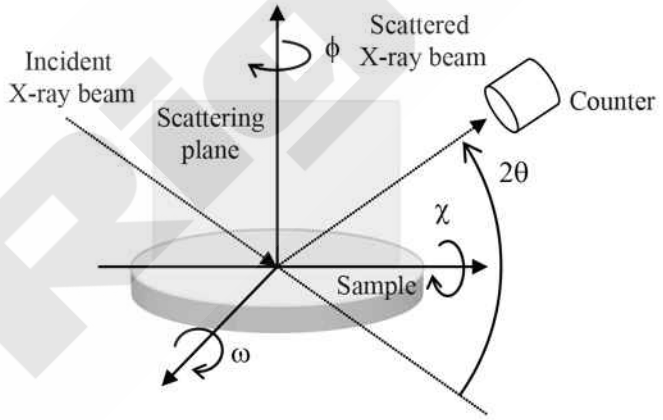


*Figure 2.4.1. Rotation axes of goniometer*

In general, a goniometer with four rotation axes (three for rotating the sample and one for rotating the counter) is called a **four-circle goniometer**. The rotation axis corresponding to the incident angle of the X-ray beam in the scattering plane is called the $\omega$ axis. The rotation axis (swing axis) perpendicular to the scattering plane is called the $\chi$ axis. The rotation axis for the in-plane rotation of the sample is called the $\phi$ axis. By rotating these three axes, we can orient the sample to any desired angle. The rotational angle of the counter with respect to the incident X-ray beam, or the diffraction angle, is called the $2\theta$ axis.

Fig. 2.4.2 shows the relationship between the axes indicated in Fig. 2.4.1 in the reciprocal space.

## 2.4 Reciprocal Lattice and Measurement Axes

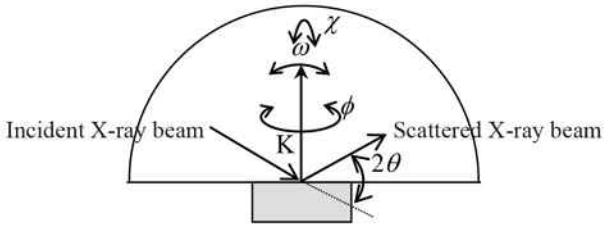


*Figure 2.4.2. Relationship between axes in reciprocal space*

Fig. 2.4.2 shows the scattering plane, including incident and scattered X-ray beams. Section 4.3.1 stated that we can measure diffraction by a reciprocal lattice point on the scattering plane if the appropriate incident angle and scattering angle are selected. However, measurements by the reflection method face the limitations described below with respect to the range that can be measured.

For example, when we measure a thin-film sample on a substrate, we must select a lattice plane so that the X-ray beam enters and exits from the surface. By doing so, we obtain sufficiently strong diffracted X-ray intensity. When the incident and exit angles are restricted in this manner, an ordinary four-circle goniometer has **blind regions** on the scattering plane in the reciprocal lattice in which measurement cannot be performed.

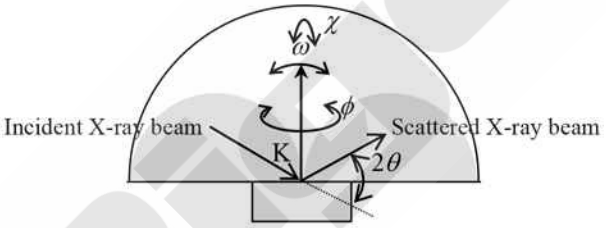


*Figure 2.4.3. Blind regions*

The two semi-circular shadowed regions shown in Fig. 2.4.3 are blind regions. If we try to measure reciprocal lattice points in these regions, the geometry requires the incident X-ray beam to enter the sample from the side or rear of the sample (semi-circular region on the left) or the scattered X-ray beam to exit the sample from the side or rear of the sample (semi-circular region on the right).

To observe reciprocal lattice points in these blind regions, we need to rotate the $\chi$ and $\phi$ axes and move the reciprocal lattice points to the observable region (out of the blind regions).

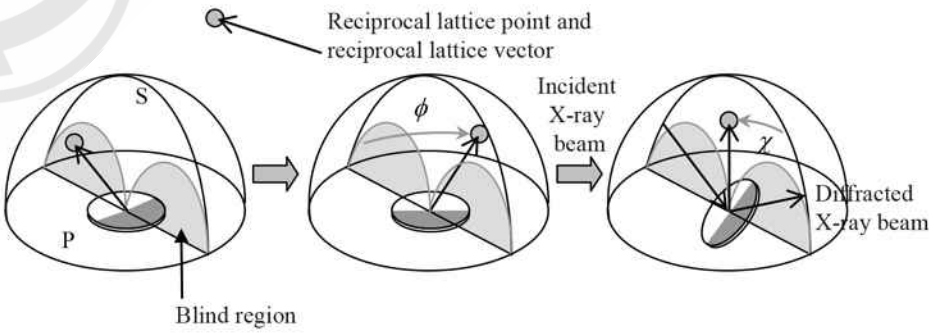


S: Scattering plane P: Plane perpendicular to scattering plane and passing though the origin

*Figure 2.4.4. Moving reciprocal lattice points to observable region*

As shown in Fig. 2.4.4, we can move a reciprocal lattice point out of the blind regions by rotating the $\phi$ axis (sample in-plane rotation axis). We can then place the reciprocal lattice point on the scattering plane once again by rotating the $\chi$ axis (sample swing axis). In this way, we can measure reciprocal lattice points in the observable region in the scattering plane in a geometry in which X-rays enter and exit from the surface of the sample.

However, if we measure a reciprocal lattice point as described above, we must rotate the sample swing axis through a large angle. Here, if we use a line-shaped X-ray beam, we confront the problem of incident X-ray beams irradiating out of the sample. This effect is especially marked if we measure the reciprocal lattice points in a part of the blind region near the plane perpendicular to the scattering plane and passing through the origin (P in Fig. 2.4.4). The reciprocal lattice point to be used in measurement must be selected with care.

## 2.4.2 Goniometer for In-Plane Measurement

Now we will discuss a goniometer that resolves the problem of incident X-ray beams irradiating out of the sample when we rotate the sample through the swing angle. This goniometer is used in measurements to extract precise data on the sample surface and interfaces (in-plane measurements).

Fig. 2.4.5 shows the rotation axes of the in-plane goniometer.

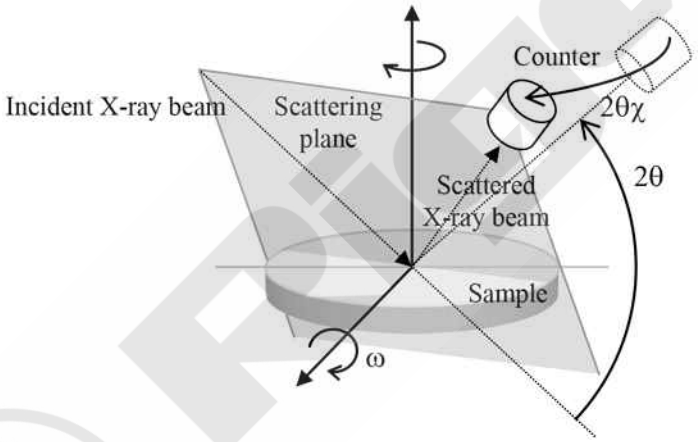


***Figure 2.4.5. Rotation axes of in-plane goniometer***

The in-plane goniometer rotates the counter around the axis perpendicular to the axis of the $2\theta$ rotation. This corresponds to pulling the counter to the front instead of repositioning the sample to face the front by tilting it 90°. This axis resolves the problem of incident X-ray beams irradiating out of the sample encountered in measurements with large sample swing angles (i.e., with a large $\chi$ axis). To enable this type of measurement, the in-plane goniometer adds a $2\theta\chi$ axis to the counter to supplement the $2\theta$ axis.

This goniometer makes it possible to measure the reciprocal lattice points in the plane perpendicular to the scattering plane and passing through the origin (P in Fig. 2.4.4) as well as reciprocal lattice points in the blind regions. This measurement technique is called **in-plane measurement**, since it measures the diffraction that occurs in the in-plane direction of the sample surface.

## 2.4 Reciprocal Lattice and Measurement Axes

Here, Fig. 2.4.6 helps clarify why the $2\theta\chi$ axis has the same function as the $\chi$ axis in the sense that it moves a reciprocal lattice point to an observable region (moves it out of the blind regions) and places it once again on the scattering plane. Fig. 2.4.6 shows the relationship in reciprocal space between the rotation axes indicated in Fig. 2.4.5. Compared to the four-circle goniometer in Fig. 2.4.2, the $\chi$ axis that rotates the sample corresponds to the $2\theta\chi$ axis that rotates the scattering plane. To observe a reciprocal lattice point, the reciprocal lattice point must be placed on the scattering plane. Here, it does not matter whether the sample (the reciprocal lattice itself) or the scattering plane is rotated as the counter is rotated. The former corresponds to the ordinary four-circle goniometer; the latter corresponds to the in-plane goniometer.

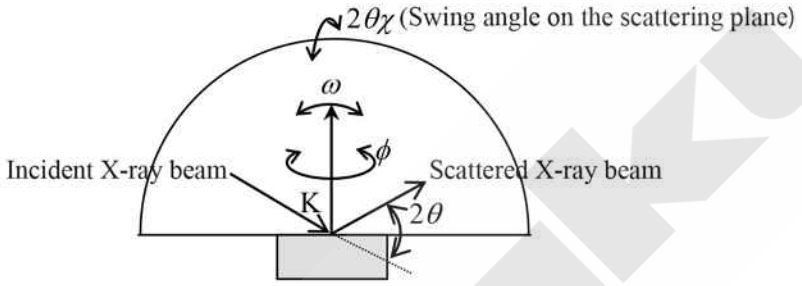


*Figure 2.4.6. Relationship between axes in reciprocal space*

Now we will consider a method for measuring the reciprocal lattice points in the blind regions described in Section 4.4.1. As described previously, the in-plane goniometer does not require swinging the sample with respect to the incident X-ray beam, rotating the counter instead. Fig. 2.4.7 shows this mechanism in a manner comparable to Fig. 2.4.4.

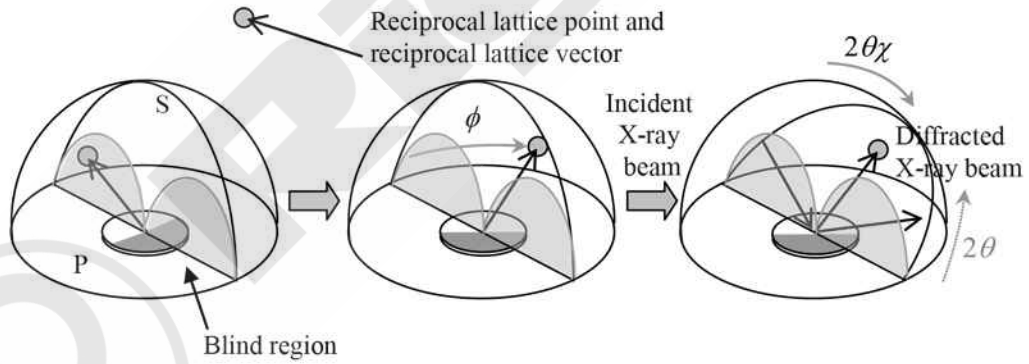


*Figure 2.4.7. Moving reciprocal lattice points to the observable region*

As shown in Fig. 2.4.7, we can move a reciprocal lattice point out of the blind regions by rotating the $\phi$ axis (sample in-plane rotation axis). Then, we can place the reciprocal lattice point once again on the scattering plane by rotating the $2\theta\chi$ axis (the rotation axis perpendicular to the $2\theta$ rotation of the counter) and thus the scattering plane, rather than by rotating the reciprocal lattice point. In this way, the reciprocal lattice points in the observable region in the scattering plane can be measured in a geometry in which the X-rays enter and exit from the surface of the sample.

When we measure the reciprocal lattice points as described above, we do not need to rotate the sample swing axis. This resolves the problem whereby the incident X-rays irradiate the sample from a tilted axis and pass out of the sample.

## 2.4.3 Reciprocal Space Coordinates

As discussed previously, we can identify the positions and shapes of the reciprocal lattice points by measuring the diffraction intensity while scanning the measurement axes in various directions. The position of the reciprocal lattice point, G (*hkl*), is the end position of the reciprocal lattice vector expressed by Formula (2.1.9). To express the position and shape of G (*hkl*) in reciprocal space, we sometimes use Cartesian coordinates ($q_x$, $q_y$) in the reciprocal space instead of measurement axes such as $2\theta$ and $\omega$. This coordinate system is called the **q coordinates** or **reciprocal space coordinates**.

We define the $\mathbf{q}_x$ and $\mathbf{q}_y$ axes as shown in Fig. 2.4.8 and consider the relationship between P ($q_x$, $q_y$) and the angular position, ($2\theta$, $\omega$), specified by the incident X-ray beam $\mathbf{k}_o$ and scattered X-ray beam $\mathbf{k}_g$. First, length q of the scattering vector is given by the following formula:

$$|q| = k_o \sin(2\theta/2) + k_g \sin(2\theta/2) = \frac{2}{\lambda}\sin\theta \qquad \textit{Formula 2.4.1}$$

The angle $\delta$ between the sample surface normal and the scattering vector is $\delta = \frac{2\theta}{2} - \omega$. Thus, $q_x$ and $q_y$ are given by the following formulas:

$$q_x = \frac{2}{\lambda}\sin\frac{2\theta}{2}\sin(\frac{2\theta}{2} - \omega)$$
$$q_y = \frac{2}{\lambda}\sin\frac{2\theta}{2}\cos(\frac{2\theta}{2} - \omega) \qquad \textit{Formula 2.4.2}$$

Formula (2.4.2) can also be expressed as follows by summing the *x* and *y* components of $\mathbf{k}_o$ and $\mathbf{k}_g$.

$$q_x = \frac{1}{\lambda}\{\cos\omega - \cos(2\theta - \omega)\}$$
$$q_y = \frac{1}{\lambda}\{\sin\omega + \sin(2\theta - \omega)\} \qquad \textit{Formula 2.4.3}$$

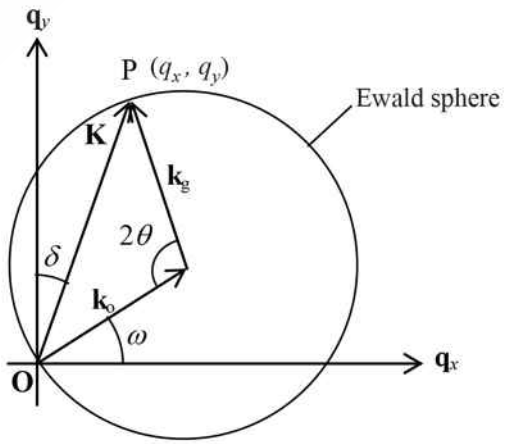


*Figure 2.4.8. Reciprocal space coordinates*

## 2.5 Reciprocal Lattice and Resolution of Optics

Measurement resolution has several possible meanings. Resolution can be roughly classified as follows:

1. Resolution of incident optics: Angular divergence and wavelength dispersion of incident X-ray beam
2. Resolution of receiving optics: Resolution of the angle and wavelength on the side receiving the scattered X-ray beam
3. Resolution of goniometer: Minimum rotation angle of each axis (Minimum step)
4. Resolution of measurement position: area irradiated by X-rays and depth (irradiated volume)

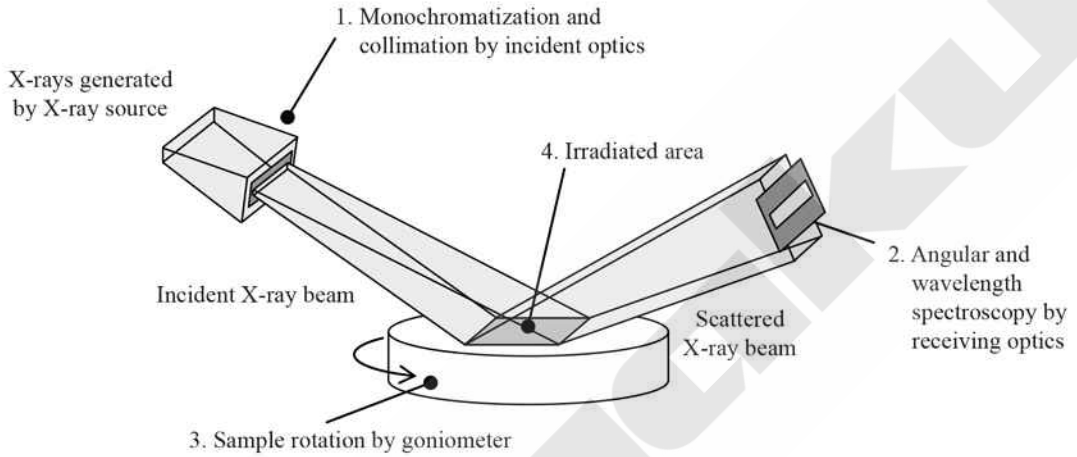


*Figure 2.5.1. Measurement resolution*

Among resolutions 1 to 4, the definitions of resolutions 1 to 3 are crucial for reciprocal space. Although resolution 4 may be defined in the reciprocal space by the size of the crystal, the X-ray irradiated volume in this sense is generally extremely large and the reciprocal lattice point corresponding to this volume can be regarded as a dimensionless point.

This section discusses how resolutions 1 to 3 relate to measurements of the reciprocal lattice—that is, to diffraction measurement.

### 2.5.1 Resolution of Incident Optics

We begin by considering 1 the resolution of the incident optics.

The angular divergence of the incident X-ray beam as specified by incident optics such as the slit and the monochromator can be expressed in real space as shown in Fig. 2.5.1 and in reciprocal space as shown in Fig. 2.5.2.

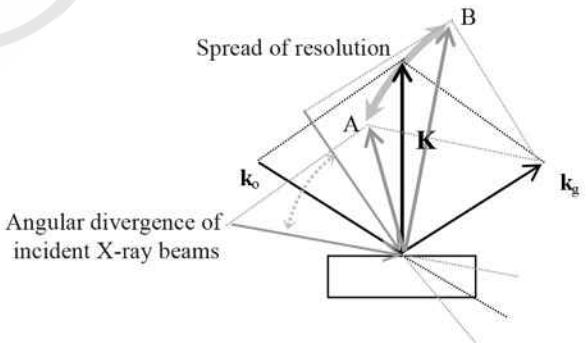


*Figure 2.5.2. Angular divergence of incident X-ray beam*

If the incident X-ray beam has an angular divergence, the resolution in reciprocal space spreads in the direction indicated by the arrow in Fig. 2.5.2. That is, incident X-ray beams entering the sample at smaller and larger angles simultaneously undergo scattering corresponding to points A and B, respectively. Here, the reciprocal lattice point is observed to spread between points A and B.

Now we consider the wavelength dispersion of the incident X-ray beam as specified by incident optics such as the slit and the monochromator. This wavelength dispersion can be expressed in real space as shown in Fig. 2.5.1 and in reciprocal space as shown in Fig. 2.5.3.

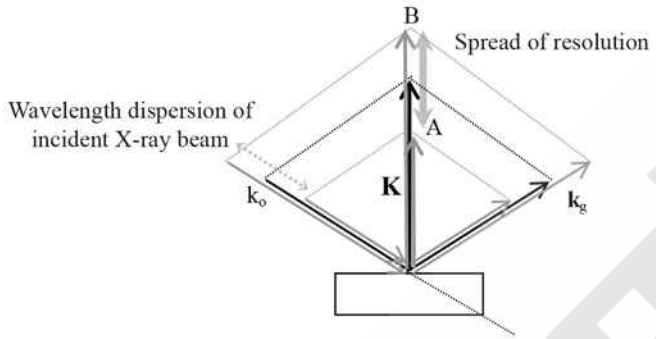


*Figure 2.5.3. Wavelength dispersion of incident X-ray beam*

If the incident X-ray beam is characterized by wavelength dispersion and the receiving optics lack sufficient resolution to monochromatize the dispersion for counting, the reciprocal lattice point spreads in the direction indicated by the arrow in Fig. 2.5.3. That is, incident X-ray beams with a longer wavelength (a shorter wave vector) and a shorter wavelength (a longer wave vector) simultaneously undergo scattering corresponding to points A and B, respectively. Here, the reciprocal lattice point is observed to spread between points A and B.

## 2.5.2 Resolution of Receiving Optics

Now we consider 2., the resolution of the receiving optics.

The receiving angular width of the scattered X-ray beam as specified by receiving optics such as the slit and the analyzer can be expressed in real space as shown in Fig. 2.5.1 and in reciprocal space as shown in Fig. 2.5.4.

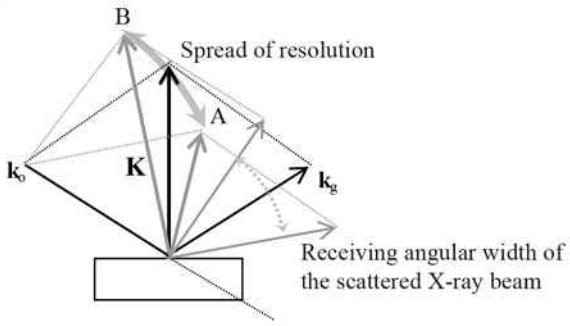


*Figure 2.5.4. Receiving angular width of the scattered X-ray beam*

# 2.5 Reciprocal Lattice and Resolution of Optics

If the receiving optics simultaneously receive scattered X-ray beams of different scattering angles, the resolution in the reciprocal space spreads in the direction indicated by the arrow in Fig. 2.5.4. That is, the scattered X-ray beam with a smaller scattering angle corresponding to point A and the scattered X-ray beam with a larger scattering angle corresponding to point B are simultaneously received. Here, the reciprocal lattice point is observed to spread between points A and B.

Now we consider the receiving wavelength resolution of the scattered X-ray beam as specified by receiving optics such as the slit and the analyzer. This wavelength resolution can be expressed in real space as shown in Fig. 2.5.1 and in reciprocal space as shown in Fig. 2.5.5.

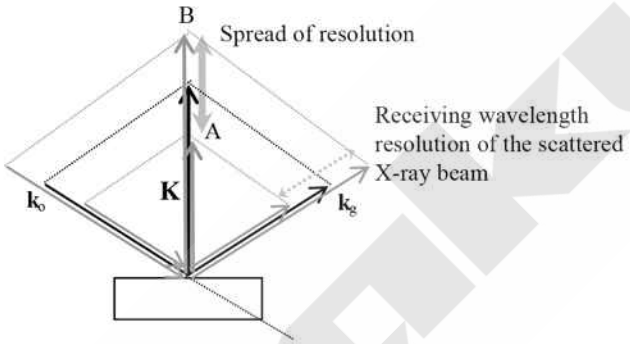


*Figure 2.5.5. Receiving wavelength resolution of the scattered X-ray beam*

If the incident X-ray beam is characterized by wavelength dispersion and the receiving optics have sufficient width in resolution to monochromatize the dispersion for counting, the reciprocal lattice point spreads in the direction indicated by the arrow in Fig. 2.5.5. That is, the incident X-ray beams with longer wavelength (shorter wave vector) and shorter wavelength (longer wave vector) simultaneously undergo the scattering corresponding to points A and B, respectively, and are counted simultaneously in the width of the wavelength resolution of the receiving optics. Here, the reciprocal lattice point is observed to spread between points A and B.and in reciprocal space as shown in Fig. 2.5.5.

## 2.5.3 Resolution Function

As determined in the previous section, if the resolution of the incident or receiving optics decreases, scattering in a region in reciprocal space is simultaneously observed. When this happens, even if the true reciprocal lattice point is an extremely small point, the reciprocal lattice point is observed with a spread corresponding to the resolution. This region in which the scattering is simultaneously observed is called the **resolution function**. The size and shape of the resolution function depends on the optics used in the measurement. The results of the investigation of the previous section show that the size and shape of the resolution function is related to the resolution of the optics shown in Fig. 2.5.6.

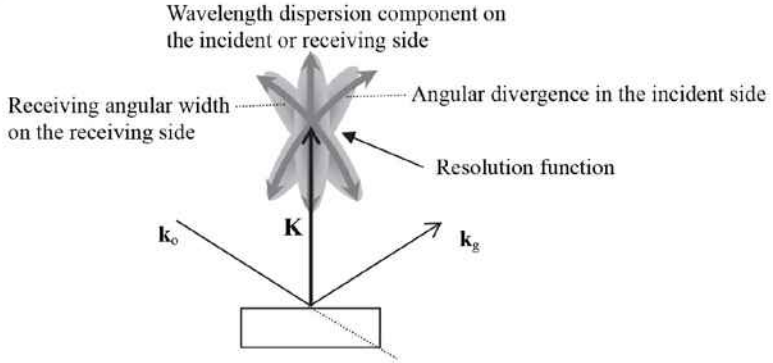


*Figure 2.5.6. Resolution function*

As shown in Fig. 2.5.6, even if we measure a sample of extremely high crystallinity and sufficient size, if the resolution function spreads across a wide range, the reciprocal lattice points of that sample will not be small points but will instead be observed to spread like the resolution function.

The discussion in Section 4.3 indicates that the reciprocal lattice point spreads as shown in Fig. 2.5.7 with changes in crystal structure or degradation in crystallinity attributable to changes or fluctuations in the crystal orientation or the lattice constants.

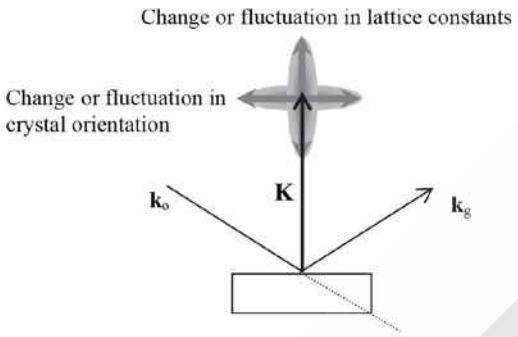


*Figure 2.5.7. Change in crystal structure and degradation in crystallinity*

Here, to accurately measure the change in the position or spread of the reciprocal lattice point due to a change in crystal structure or degradation in crystallinity, we must use a resolution function that is sufficiently small relative to this change or spread. The optics for various measurements can be determined from the relationship between the size of the reciprocal lattice point to be measured and the resolution function of the measurement.

## 2.5.4 Resolution of the Goniometer

Scanning by rotating the axes of the goniometer corresponds to measuring the scattering intensity while scanning the reciprocal space using a resolution function of a specific size, as shown in Fig. 2.5.8.

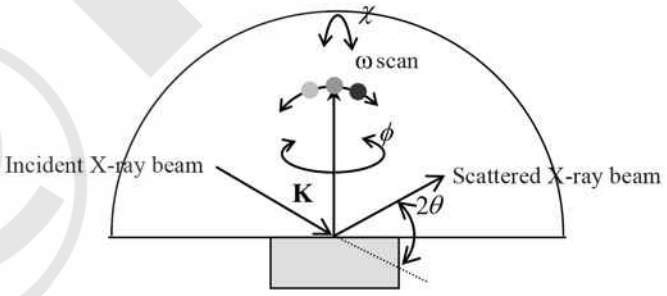


*Figure 2.5.8. Scanning of goniometer axes (for ω axis)*

## 2.6 Single Crystal and Polycrystal

So far, we have assumed that the sample is a single crystal in our discussion of the concept of the reciprocal lattice. However, the actual sample may be a single crystal with fluctuations in orientation, a polycrystal with a fiber orientation only, or a randomly oriented polycrystal with no orientation. How do we express the reciprocal lattice of a polycrystal with a fiber orientation or of a completely random polycrystal?

Fig. 2.6.1 schematically shows the reciprocal lattice of each of the samples above.

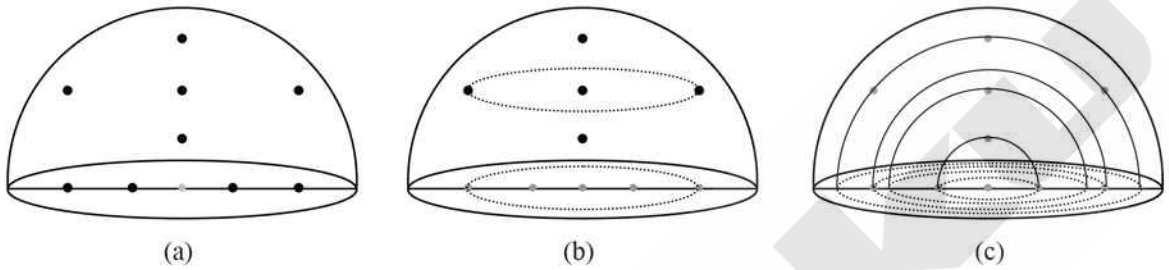


***Figure 2.6.1. Reciprocal lattice of (a) single crystal; (b); oriented polycrystal; and (c) random polycrystal***

As implied by Fig. 2.6.1, the appearance of the reciprocal lattice changes depending on whether the sample crystal is a single crystal or a polycrystal and whether it has an orientation. The orientation of crystallites in a polycrystal is generally not uniform; a polycrystal contains crystallites oriented in various directions. This means the reciprocal lattice points are no longer points. For samples with a fiber orientation, a reciprocal lattice point forms a circle around the axis of the preferred orientation. If the sample is a random polycrystal with no orientation, the circle spreads to a sphere of fixed radius. The radius of the sphere equals the inverse of the interplanar spacing.

## 2.7 Summary

This chapter defined and discussed the concept of the reciprocal lattice and its physical meanings. It also discussed the relationship between the reciprocal lattice and various measurement techniques, goniometers, and optical resolution. Summarized below are the major definitions and other issues discussed in this chapter.

1. Definition of reciprocal lattice

   Direction of lattice planes (hkl): Identical to the normal to the lattice planes as drawn from the origin

   Length of lattice planes (hkl): Equal to the inverse of the interplanar spacing dhkl.

   Reciprocal lattice vector: $\mathbf{g}_{hkl} = h\mathbf{a}^* + k\mathbf{b}^* + l\mathbf{c}^*$

   $\mathbf{a}^* = \mathbf{b} \times \mathbf{c},\ \mathbf{b}^* = \mathbf{c} \times \mathbf{a},\ \mathbf{c}^* = \mathbf{a} \times \mathbf{b}$

   Diffraction condition: $\mathbf{k}_g - \mathbf{k}_o = \mathbf{g}_{hkl}$

2. Relationship between reciprocal lattice and crystal structure

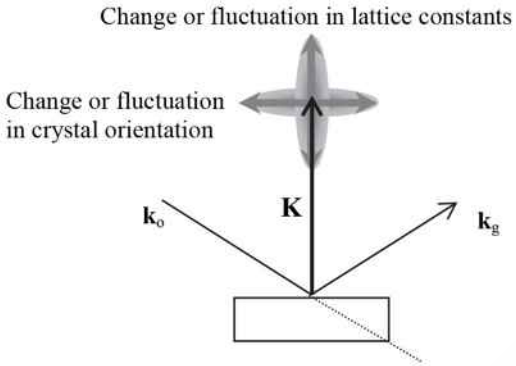


3. Relationship between reciprocal lattice and goniometer axes

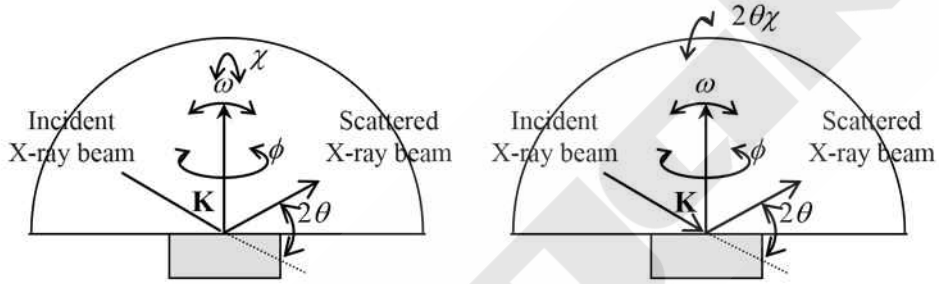


***Ordinary four-circle goniometer*** ***In-plane goniometer***

4. Relationship between reciprocal lattice and resolution of measurement

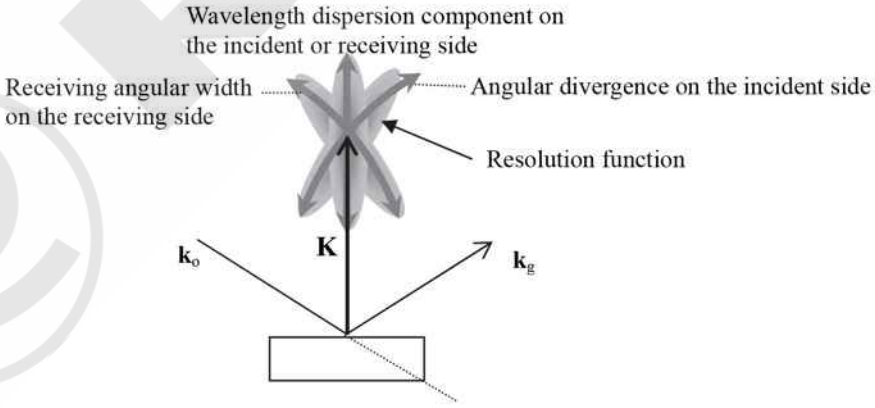

Rigaku

# THE BRIDGE

**MATERIALS ANALYSIS eNEWSLETTER**

MARCH 2014, ISSUE 9